Optically Defined Reconfigurable THz Metasurfaces using Graphene on Iron-Doped Lithium Niobate

Jon Gorecki,* Adnane Noual, Sakellaris Mailis, Vasilis Apostolopoulos, and Nikitas Papasimakis

Graphene plasmonic devices have been demonstrated to show great potential for reconfigurable metasurfaces due to the tuneable electronic charge transport properties of graphene in response to electrostatic gating. Iron-doped lithium niobate is proposed as a platform for patterning-free optically reconfigurable graphene metasurfaces in the THz spectral region. Under structured illumination, the lithium niobate undergoes charge migration in the bulk, where carriers migrate away from illuminated regions, forming spatially patterned charge distributions capable of electrostatic tuning of graphene. These charge distributions are stable in the dark, however, can be redefined by subsequent illumination. Through the use of numerical simulations, it is demonstrated that optically defined charge distributions in lithium niobate can tune locally the graphene Fermi level allowing for plasmonic resonances at THz frequencies.

1. Introduction

Plasmonic devices have proven themselves to be extremely useful for the control of terahertz frequency radiation, providing methods for spatial filtering,[1] control of incident wave transmission,[2–6] phase,[7–10] polarization,[11–13] and the coupling between guided modes and free space.[14] Recently graphene plasmonic devices have been shown to have great potential for a multitude of optoelectronic applications due to the inherent ultra-high mobility values,[15] extreme spatial confinement of plasmons,[16,17] and controllable Fermi level,[18] which make graphene to be a highly adaptive platform for plasmonic devices.[19,20] The plasmonic resonance frequency can be derived from a Drude model and shown to depend on the Fermi level instead of the usual dependence on effective carrier mass. Further, the plasma resonance frequency has been shown to be tuned by controlling the Fermi level through the electrostatic gating of the graphene.[21] Because of the high carrier mobility values in graphene, the plasmonic resonances can be sustained in the terahertz[21] and beyond into the infrared[22,23] regime.

There are two common methods followed for plasmonic resonances in graphene devices; first, the graphene can be patterned to form ribbons or split ring resonators to sustain a plasmonic resonance,[21] while the second less explored method utilizes a continuous graphene layer which is periodically doped to sustain a resonance mode. The first method has been demonstrated via a range of techniques such as graphene strips on a silicon on insulator substrate tuned with an ion-gel gate[21]; chemical doping via atmospheric gasses of graphene patterned into disk arrays,[24] and for graphene patterned into split ring resonators (which allows for a longer resonance path to be wrapped into a unit cell and avoid diffraction).[25–28]

The second method of graphene plasmonics has been much less explored in the literature and so far has proved difficult to demonstrate experimentally. This method utilizes periodic variations in the Fermi level of a graphene layer to allow for the existence of plasmonic resonance modes. Theoretical analysis of a graphene layer with variations in Fermi level has been shown for structures of ribbons[29] and disks,[30] where the authors observe that by patterning graphene with a suitable Fermi level geometry plasmonic resonances can be sustained at terahertz frequencies. However, although these resonances

J. Gorecki
School of Engineering and Material Science
Queen Mary University of London
London E1 4NS, UK
E-mail: j.gorecki@qmul.ac.uk

A. Noual
Département de Physique
Université Mohammed Premier
Oujda 60000, Morocco

S. Mailis
Center for Photonic Science and Engineering
Skolkovo Institute of Science and Technology
Moscow 143026, Russia

V. Apostolopoulos
School of Physics and Astronomy
University of Southampton
Southampton SO17 1BJ, UK

N. Papasimakis
Optoelectronics Research Centre
University of Southampton
Southampton SO17 1BJ, UK

can be demonstrated in simulations, questions still remain as to how such Fermi-level variations could be practically achieved. One suggestion involves the deposition of graphene on a trenched silicon substrate to induce Fermi-level changes which can create conditions for waveguiding.[31] One group has demonstrated experimentally transparent metal oxide and organic gates[32,33] patterned into ribbons covered with a top layer of graphene. The gates induce a periodic tuning effect in the graphene, which can then sustain terahertz frequency resonances. Another method is to place a graphene layer on a periodically poled ferroelectric substrate, which has been shown via simulations to create a structured Fermi-level profile within the graphene due to electrostatic interactions with the substrates, and is capable of sustaining plasmonic resonances.[34–38] This method of using ferroelectric substrates has made modest progress experimentally, as spatially resolved Raman spectroscopy of graphene on poled lithium niobate has been shown to introduce a periodic variation in the graphene Fermi level[39]; however, plasmonic resonances were not demonstrated. Reconfigurable tuning of 2D materials can be achieved by rewriting ferroelectric domains with an atomic force microscopy (AFM) tip, however, this is a slow process and limited to small areas. Furthermore, this technique requires close proximity contact to the device.[40]

Lithium niobate is an attractive substrate for this electrostatic tuning of graphene as it supports spatially resolved sub-micron-scale charge distributions, which can be imprinted on the crystal by spatially selective optical illumination in a nonvolatile, yet optically rewrite-able fashion.[41,42]

In our previous work in 2018,[43] we demonstrated experimentally the graphene on iron-doped lithium niobate as a platform for nonvolatile optical control of graphene electrical resistivity, capable of altering the charge carrier numbers by 5.5×10^{-12} cm^{-2}, resulting in an estimated Fermi energy increase of 0.3 eV in the graphene. In this work, we characterized the graphene via Raman spectroscopy to confirm its monolayer thickness and absence of defects, and performed measurements of the electrical resistance of the device with an Agilent probe station in response to optical illumination. Following on from this, in 2020,[44] we published an experimental demonstration of the graphene on iron-doped lithium niobate platform for

tuning of THz frequency resonances by incorporating a metallic metasurface sandwiched between the graphene and lithium niobate. The effect was demonstrated to be nonvolatile yet reversible upon the application of heat. The transmission properties of the device were characterized extensively by THz time-domain spectroscopy (TDS), both in the dark and under illumination from a coherent light source.

In this work, we show through numerical simulations that graphene on iron-doped lithium niobate can allow for resonator geometries to be patterned simply by structured optical illumination of the device creating nonvolatile tuning of the graphene enabling resonator structures to be created, which could be reversed by uniform illumination of the substrate and redefined at will. Our simulations show that the device supports resonances at THz frequencies when ribbon or split ring resonator patterns are used.

2. Material Parameters

In this work, we investigate through the use of finite element simulations the spatially resolved Fermi energy tuning of a graphene mono-layer on Fe:LiNbO$_3$ as shown in **Figure 1**, and probe the transmission properties of the system to THz frequency radiation. The optically induced charge migration effect in the lithium niobate substrate[41,42] (often referred to as the photorefractive effect) is depicted in Figure 1b; in response to optical illumination, a photon is absorbed by an Fe^{+2} ion located at an interband state, which excites an electron to the conduction band. Once in the conduction band, the electron is free to migrate within the crystal, being driven by either drift or diffusion, until a time when the electron has migrated to a dark region of the crystal that is not illuminated. At this point, the electron falls back to the interband state and is captured by an Fe^{+3} ion, where it becomes trapped. By this process, electrons can be made to move away from illuminated regions and collect in dark areas of the crystal. The resultant charge domains are stable in the dark at room temperature; however, can be redefined by subsequent illumination.

In this article, we investigate two cases; the 1D charge profile which creates a ribbon-like resonator system, and the 2D charge
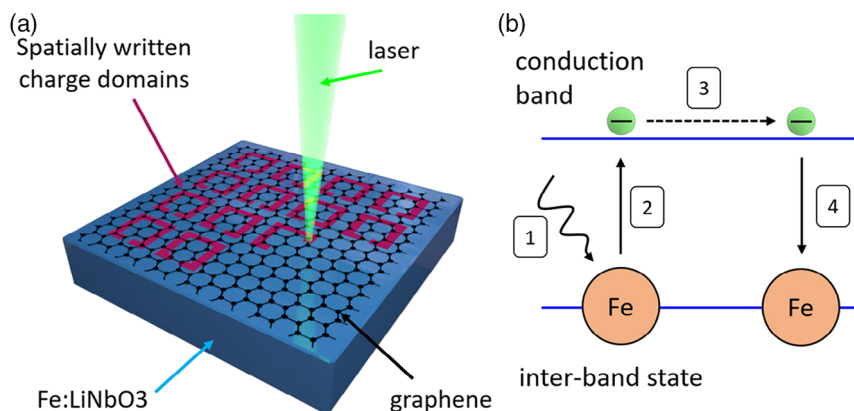

Figure 1. a) Schematic of a plasmonic device consisting of graphene on Fe:LiNbO$_3$ substrate. In response to structured illumination (depicted here as a scanning laser), the charge migration effect in the substrate will create nonuniform charge distributions, which will electrostatically tube the graphene Fermi energy. b) Depiction of the charge migration process in iron-doped lithium niobate.

profile, which creates a split-ring-resonator-type structure. To carry out simulations, it is necessary to define a parameter space for the material properties, which we discuss in the following:

2.1. Device Size

Due to the wavelength of THz frequencies, the smallest area of the device should be on the scale of several square millimeters, which therefore requires chemical vapor deposition (CVD) graphene.

2.2. Grating Periodicity

Due to the optical nature of the photorefractive effect, there is a lower size limitation on the period of the optical grating as it is not possible to structure the illumination pattern at scales smaller than the wavelength of the illumination source. The photorefractive effect is responsive to the blue/green region of the visible spectrum, and therefore the minimum feature size could be 0.5 μm.

2.3. Mobility

The largest mobility values in graphene can be obtained by suspended single crystal exfoliated sheets,[15] however, for commercially available large-area CVD films purchased from Graphenea the stated mobility values are somewhere in the region of 2000–4000 $cm^2 Vs^{-1}$ on SiO_2/Si, and increased to around 7000 $cm^2 Vs^{-1}$ on aluminum oxide. This is generally in-line with reported values of CVD graphene mobility,[45,46] however, can be increased to many tens of thousands by encapsulation with hexagonal boron nitride monolayers.[47]

2.4. Photorefractive Charge Density

To gauge the electrostatic behavior of lithium niobate, we look to the reported large electric fields ranging from several tens up to hundreds of kV cm^{-1},[48–51] which equate to surface charge densities in the range from $\times 10^{-3}$ up to $\times 10^{-2}$ C m^{-2}, which can be obtained by charge volume densities of several thousand C m^{-3}. These values are in-line with our previous report, where we found Fe:$LiNbO_3$ substrate injecting 5.5×10^{12} carriers into the graphene monolayer.[43] As our previous experiments were performed under ambient conditions, the device must have experienced a degree of atmospheric charge compensation, and therefore we suggest that under vacuum the charge carrier injection values would be somewhat larger than we observed. Here, we use a nominal value of 1,500 C m^{-3} for the charge volume density.

3. Simulation Methods

A finite element analysis method (COMSOL) is used to investigate the electromagnetic response of the system. The 2D unit cell shown in **Figure 2**a shows an air slab of width w (taken as 50 μm) with a depth of 300 μm on top of a lithium niobate slab of depth 200 μm, with another air domain below. Each of the vertical unit

cell boundaries has a periodic condition applied to model an infinite array of unit cells. At the air/lithium niobate interface is a graphene monolayer modeled as a transition boundary.

The lithium niobate slab is modeled with frequency-dependent values of complex refractive index, which we have measured via THz TDS, and reported in detail previously.[52] The graphene conductivity (σ) and scattering time (τ) are calculated from the Kubo equations[53] as shown in Equation (1) and (2), respectively

$$\sigma = \frac{ie^2 E_F}{\pi \hbar^2 (\omega + i/\tau)} \tag{1}$$

$$\tau = \frac{E_F \mu}{e v_F^2} \tag{2}$$

where e is the electron charge, t is the graphene thickness (1 nm), ω is the radial frequency, μ is the graphene charge carrier mobility, and v_F is the Fermi velocity (10^8 cm s^{-1}).

To determine the surface charge profiles created in lithium niobate due to the photorefractive effect, an electrostatic simulation is used. A schematic diagram of the 2D COMSOL model is presented in Figure 2a, which shows a slab of lithium niobate cut into two sections, where the left section is given a volume charge density of $-\rho$ while the right-hand side of the slab is given a volume charge density of $+\rho$. The bottom surface of the lithium niobate is grounded. The electrostatics module in COMSOL is solved to obtain the charge density at the top surface of the lithium niobate.

The charge density profile calculated in COMSOL at the top surface of the lithium niobate is converted into an electron number density per cm^2 to determine the number of electrons which will be injected into the graphene sheet in response to the electrostatic interaction with the substrate (assuming a one to one correlation of carriers). Figure 2b presents the number of carriers injected into the graphene as a function of spatial dimension $\hat{x}$ along the 50 μm wide unit cell for several values of volume charge density ρ. The carrier density displays a sinusoidal profile across the $\hat{x}$ dimension, and when increasing the value of ρ the magnitude of the sinusoidal profile is increased. In the inset figure in the top left, the magnitude of the sinusoidal profile (Δn) is plotted against ρ revealing a linear relation, where a volume charge density of several kC m^{-3} is capable of injecting $\times 10^{13}$ cm^{-2} carriers, which for graphene constitutes a significant carrier injection.

Figure 2c presents an example graph showing the relation of Fermi level to charge carrier numbers, where the Fermi level has a minimum value at zero carriers and increases sub-linearly with an increasing absolute number of carriers (either electrons or holes). Typical values of Fermi level and carrier densities for graphene are energies up to 1.0 eV, and carrier densities up to $\times 10^{13}$ cm^{-2}. The graph shows the example of a graphene sheet starting with n carriers, which experiences an injection/ejection of Δn carriers, which results in the creation of two new Fermi level values. The difference in Fermi level values is termed ΔE_F.

Figure 2d reveals the Fermi level changes which can be achieved in response to the electrostatic tuning of the substrate. The initial Fermi energy of the graphene is set to be positive (p doped) as CVD graphene is generally always intrinsically p-doped due to its manufacturing process. The Fermi level difference (ΔE_F) is plotted against the initial Fermi level, and carrier

**ADVANCED
SCIENCE NEWS**

www.advancedsciencenews.com

**ADVANCED
PHOTONICS
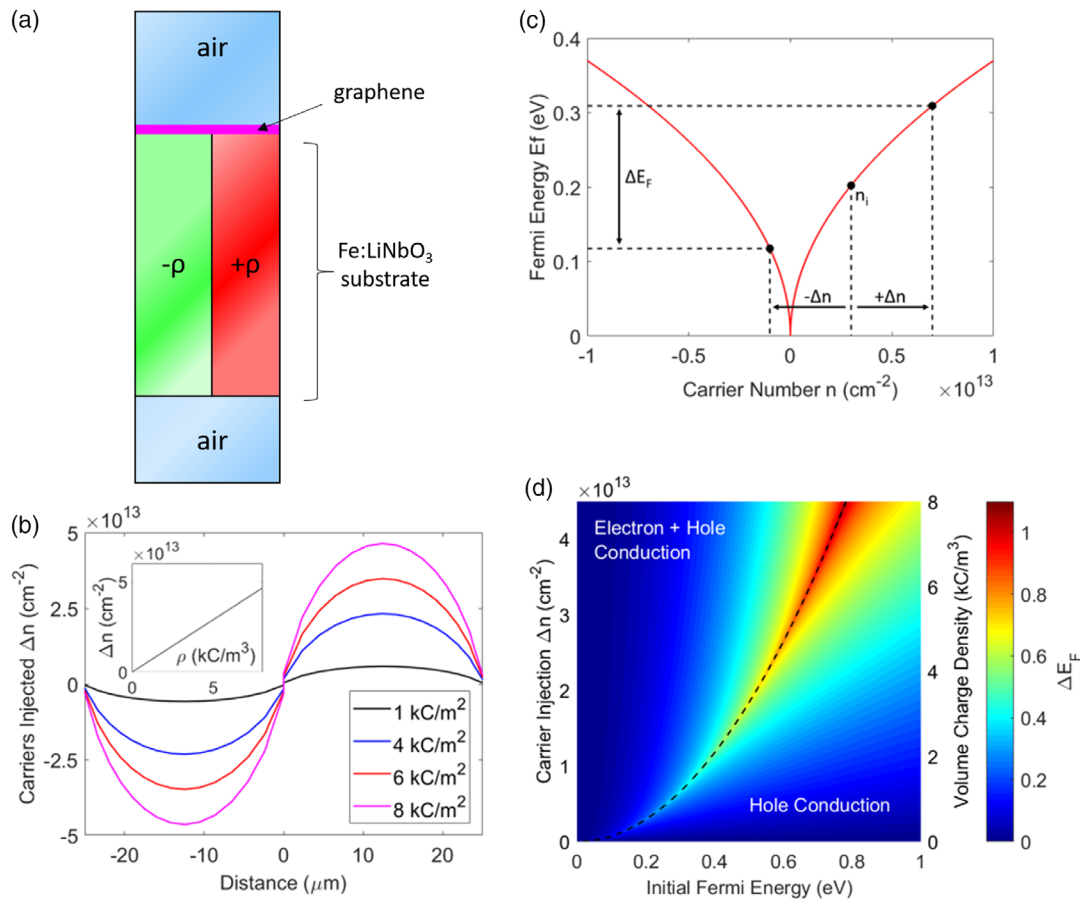RESEARCH**

www.adpr-journal.com

Figure 2. a) Schematic of the 2D unit cell, consisting of air slab followed by lithium niobate split into two regions of positive and negative space charge density. A graphene monolayer covers the top surface of the lithium niobate. b) Spatially varying photo-induced carrier density change in graphene sheet determined via electrostatic simulations of charge volume densities in lithium niobate. c) Relation of Fermi level to carrier density. d) Fermi level change as a function of carrier density and initial Fermi energy.

injection (Δn). It can be seen that all initial Fermi energies with zero carrier injection begin in the hole conduction regime, however, as carriers are injected the ΔE_F increases, and can pass into the regime where one region of the graphene is conducting with holes, and the other region of the graphene is conducting with electrons. The black dotted line shows the position of the maximum Fermi energy difference, which is achieved when one region of the graphene reaches a Fermi energy of 0 eV.

4. 1D Patterning

Figure 3a presents the graphene carrier number injection (Δn) and Fermi level as a function of the spatial dimension $\hat{x}$ in response to the electrostatic interaction with a lithium niobate substrate, where the substrate in the central $\pm 12.5\,\mu m$ region is held at a volume charge density of $-\rho$ while the outside region is held at $+\rho$ (ρ is set to 1500 C m^{-3}). The initial Fermi energy of the graphene is 0.4 eV in the hole conducting regime. The width of the unit cell ($w = 50\,\mu m$) is chosen to provide a resonance response in the THz spectral region. It can be seen from the carrier injection (left-hand $\hat{y}$ axis in red) that in the center (0 μm) the

graphene experiences carrier injections of $1 \times 10^{13}\,cm^{-2}$ holes while at the edges this behavior is reversed and there is carrier ejection of $1 \times 10^{13}\,cm^{-2}$. The blue line plots the Fermi level of the graphene, where it can be seen that the addition of holes in the central region raises the Fermi level to near 0.5 eV while at the edges the Fermi level falls to around 0.05 eV, corresponding to a central ribbon of highly conducting graphene surrounded by low conductivity graphene on each side. A schematic diagram is shown inside the figure depicting the side view of the unit cell, where the incident electric field is linearly polarised along the $\hat{x}$ axis.

THz transmission through the unit cell is shown in Figure 3b for a range of carrier injection values. The transmission values are normalized against transmission through an identical air/lithium niobate unit cell in the absence of graphene. The initial Fermi level is set at 0.4 eV and the mobility at 10 000 cm^2 Vs^{-1}. It can be seen from the figure that as Δn is increased the transmission through the unit cell increases, and at a Δn value of $1.2 \times 10^{13}\,cm^{-2}$ a clear resonance peak can be observed around 0.28 THz.

To investigate the resonance mode in the graphene, the electric and magnetic fields (at a plane 5 μm above the graphene
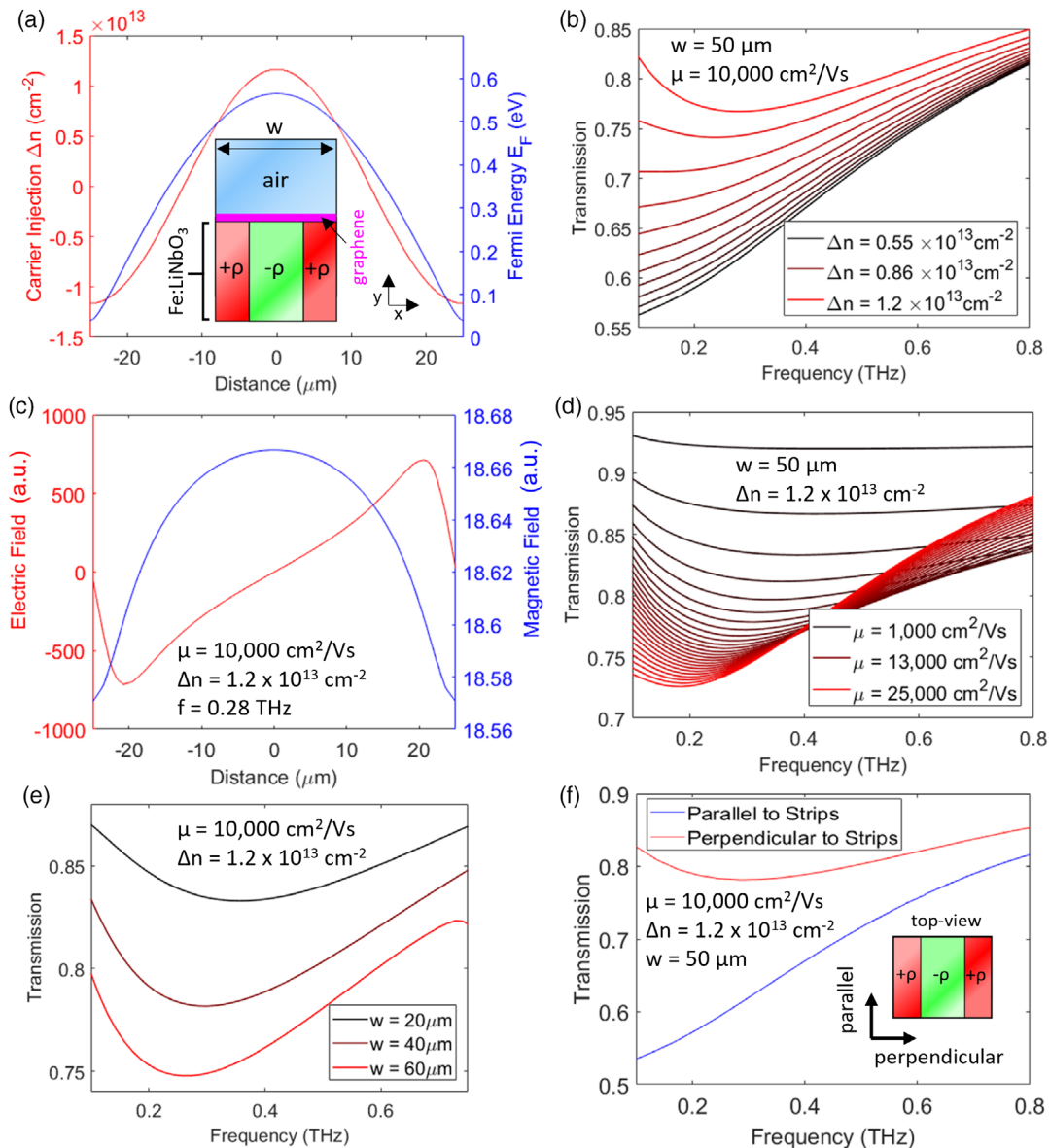
Figure 3. a) Charge density and Fermi level profile of graphene sheet, with a schematic of side-view of the unit cell where graphene is indicated by a purple line. b) Transmission spectra with varying Δn. c) Electric and magnetic fields highlighting fundamental resonance mode. d) Transmission spectra for varying mobility values. e) Transmission spectra for varying unit cell sizes. f) Transmission spectra for incident electric field parallel and perpendicular to the plasmonic grating direction.

surface) at the resonance frequency (0.28 THz) are plotted in Figure 3c. The electric field is the real part (plotted at an arbitrary phase) of the field in the $\hat{y}$ axis (vertical), which relates to regions of localized charges in the graphene. It can be seen from the electric field that there is a localization of negative charge on the left side, and a localization of positive charge on the right-hand side which will create an electric potential between these two regions. The magnetic field is the absolute part in the out-of-plane direction, which relates to electric current passing in the $\hat{x}$ direction. The figure shows magnetic fields are concentrated in the central region of the unit cell, which suggests electric currents passing along the $\hat{x}$ direction. The single central maxima of the magnetic

field, and the two electric field localizations suggest that this is indeed the profile of the fundamental resonance mode for a ribbon structure.

Figure 3d presents THz transmission spectra for a range of carrier mobility values, from 1000 to 25 000 cm^2 Vs^{-1}. In this simulation, the initial Fermi level is set to 0.4 eV while the carrier injection value (Δn is set to 1.2×10^{13} cm^{-2}, which renders the minimum Fermi level near zero. It can be seen that as the mobility increases the strength of the resonance is increased and is also red-shifted to lower frequencies, reaching a maximum peak strength around 25% at 0.2 THz when the mobility is a maximum at 25 000 cm^2 Vs^{-1}.

Figure 3e investigates the effect of unit cell size on the resonance profiles. In this simulation, the initial Fermi level is set to 0.4 eV while the carrier injection value (Δn) is set to 1.2×10^{13} cm^{-2} and mobility at 10 000 cm^2 Vs^{-1}. It can be seen that as the unit cell size increases the resonance peak grows in strength and is also red-shifted to lower frequencies. It should be noted here that to increase the unit cell size while maintaining a constant value of Δn that the space charge density ρ must also be increased.

To determine whether the transmission spectra observed here are truly due to a resonance effect (rather than simply changing the electronic properties of the graphene monolayer) the unit cell is simulated with incident THz pulses in two orthogonal linear polarisations shown in Figure 3f. In this simulation the initial Fermi level is set to 0.4 eV, the carrier injection value (Δn) is set to 1.2×10^{13} cm^{-2}, mobility at 10 000 cm^2 Vs^{-1}, and the unit cell width is 50 μm. The inset figure shows a top-down view of the unit cell with two regions of lithium niobate at high and low space charge density (ρ), with the parallel ($\overrightarrow{prll}$) and perpendicular ($\overrightarrow{prp}$) orientations denoted in the diagram. In the parallel orientation, there is no resonance mode excited, while in the perpendicular orientation the resonance mode is excited. For the perpendicular orientation where the resonance mode exists it can be seen there is higher transmission, and the presence of a resonance peak around 0.3 THz. For the parallel configuration where no resonance mode would be expected to exist, it can be seen the transmission is far lower, and that no resonance peak is observed. When excited in the non-resonant polarization in Figure 3f, the transmission is far lower than for the resonant case, and the spectra is very similar to those shown in Figure 3b for low values of Δn. This finding helps to explain the results in Figure 3b, where the transmission appears to increase as carrier injection increases. We interpret this as when the graphene has a low carrier injection (and therefore a low Fermi level contrast) there is no plasmonic resonance mode. In this scenario, the graphene absorbs the THz radiation due to free carrier absorption where the energy is lost to the surroundings. As the number of free carriers increases the plasmonic resonance appears and the graphene resonantly absorbs and re-emits the incident radiation, and therefore the transmission is higher for the case of the plasmonic resonator.

5. 2D Patterning

To exploit further the potential of lithium niobate for optically defined graphene plasmonics, we investigate whether 2D charge domain patterns in lithium niobate could be used to create more complicated structures such as a split ring resonator geometry.

A 3D model is created in COMSOL which consists of a slab of air 300 μm deep, with a square unit cell size of 50 μm. Below the air is a slab of lithium niobate also of 300 μm depth. At the air–lithium niobate interface is a sheet of graphene defined as a 2D transition boundary. The lithium niobate is split into two sections of positive and negative charge density, as shown in **Figure 4**a which creates a split ring geometry. The bottom face of the lithium niobate is grounded, and the charge volume density used here is 1500 C m^{-3} inside the ring, while the volume outside the ring is at −1580 C m^{-3}. This subtle balance

of the two values of space charge density is essential to achieve the correct Fermi level profile in the graphene to create a resonator structure that is electrically "isolated" from its surroundings. The simulation method is identical to that listed earlier except for it now utilizes a 3D model.

Figure 4b shows a surface map of the graphene Fermi level, which is created in response to the electrostatic charge distributions within the lithium niobate substrate. The split ring geometry of the lithium niobate is overlaid in black outlines. Although the graphene initially starts at 0.4 eV, it can be seen that all regions of the graphene exhibit a reduced value of Fermi level, where the highest value is 0.18 eV. This global reduction can be understood by assessing the charge distribution geometry within the lithium niobate, where an imbalance in the volume of regions at $+\rho$ and $-\rho$ will result in a net nonzero change to the graphene Fermi level. From the figure, it can also be seen there is a region of high conductivity (shown in red), which follows a split ring shape, bounded outside by lower conductivity graphene.

Figure 4c presents transmission spectra at terahertz frequencies for varying values of graphene mobility. It can be seen that with a moderate value of 10 000 cm^2 Vs^{-1} there is the presence of a resonance absorption centered around 0.3 THz, however, this is a fairly weak resonance reaching only a few percent absorptions. As the mobility is increased, it can be seen that the resonance increases in strength and also red-shifts to lower frequencies. Mobility values are further investigated by sweeping mobility values from 5000 to 20 000 cm^2 Vs^{-1} over 50 steps, and the relation of the transmission (T) to the frequency (f) is fitted via a least-squares method to a Gaussian resonance equation as shown in Figure 4. The parameter b, which corresponds to the central resonance frequency, is plotted in the black line, showing that the resonance frequency decreases as the mobility increases. The parameter c, which corresponds to the resonance width, is plotted as a patch where the width of the patch depicts the width of the resonance peak. The resonances investigated here display broad resonance peaks with widths around 1 THz. The parameter a corresponds to the magnitude of the resonance mode, and is plotted as a color scale. It can be seen that the resonance magnitude is extremely weak at low mobility values (0.02) and as the mobility increases the resonance magnitude increases by a factor of 3.

The central resonance frequency is plotted against graphene mobility. The resonance frequency is obtained by finding where the derivative of the transmission with respect to frequency is equal to zero. It can be seen that as the mobility increases there is a near linear decrease in the location of the resonant frequency, which disappears from within the available frequency window by a mobility value of 30 000 cm^2 Vs^{-1}. This result is expected, as when the graphene mobility increases there is a proportional increase to the carrier lifetime (τ), which means the plasmonic mode can sustain a longer resonance time period, equating to shorted lower frequency oscillations.

The achievable modulation depth with this scheme, as shown in Figure 4c, is able to reach 6% at resonance frequency with a graphene mobility value of 20 000 cm^2 Vs^{-1}. It is shown in the figure that the modulation depth increases as the graphene mobility increases, where mobility values are plotted in the range of 5000–20 000 cm^2 Vs^{-1}. To provide the context in practical terms, the value of 20 000 cm^2 Vs^{-1} is at the upper end of what is currently achievable with CVD graphene, however, it may be

**ADVANCED
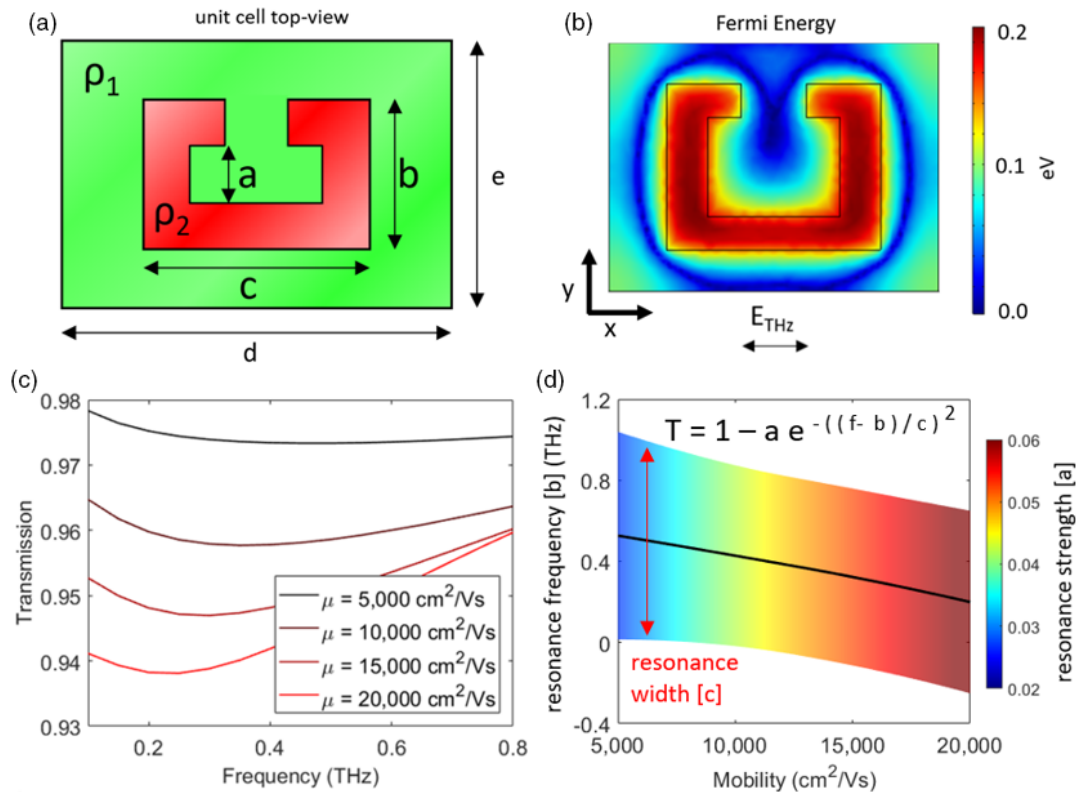SCIENCE NEWS**

www.advancedsciencenews.com

**ADVANCED
PHOTONICS
RESEARCH**
Open Access

www.adpr-journal.com

Figure 4. a) Geometry of spatial charge densities in lithium niobate where $a = 6\,\mu m$, $b = 10\,\mu m$, $c = 13\,\mu m$, $d = 20\,\mu m$, $e = 15\,\mu m$, $\rho_1 = 1580\,C\,m^{-3}$, and $\rho_2 = 1500\,C\,m^{-3}$. b) Fermi level profile of graphene sheet in eV. c) Transmission spectra for varying mobility values. d) Fitted Gaussian parameters of resonance spectra plotted against graphene mobility.

possible to utilize large area exfoliated flakes to extend this upper limit to higher mobility values.

It is likely that the resonances presented here are of low strength as we model a continuous sheet of graphene with non-zero electrical conductivity, which makes it challenging to create highly confined plasmonic resonance modes. The ideal situation would be to have regions of highly conducting graphene surrounded by non-conducting regions, which would create a tight spatial confinement of the plasmonic mode. Unfortunately, it is a fundamental property of intrinsic monolayer graphene that it has always non-zero electrical conductivity due to the absence of a bandgap. To overcome this issue, many researchers are actively looking for ways to open bandgaps in the electronic structure of graphene, which would further enhance its applicability in optoelectronic devices and field-effect transistors. Researchers have shown there are a number of methods available to open electronic bandgaps in graphene of several hundred meV, such as the use of bilayer graphene,[54] twisted bilayer graphene,[55,56] lattice symmetry breaking from substrate mismatch,[57,58] and application of mechanical strain.[59]

6. Conclusions

Optically addressed graphene plasmonics in the THz region have been demonstrated numerically in a graphene–Fe:LiNbO$_3$ hybrid arrangement, where photocarriers, generated in Fe:LiNbO$_3$, are used to modulate the charge carrier density in graphene. We model regions of volume charge density in lithium niobate via electrostatics simulations to determine charge profiles at the interface with graphene, which spatially modulates the Fermi level of graphene. We show that such an arrangement is capable of sustaining plasmonic resonances in ribbon and split ring geometries. Experimental verification of such a device would open the door to a new generation of truly reconfigurable plasmonic devices without the need for permanent patterning of structures, which can cause graphene contamination and degradation, and instead relying on optically defined carrier density modulations that can be created and redefined at will simply by structured illumination.

Conflict of Interest

The authors declare no conflict of interest.

Data Availability Statement

The data that support the findings of this study are available from the corresponding author upon reasonable request.

**ADVANCED
SCIENCE NEWS**

www.advancedsciencenews.com

**ADVANCED
PHOTONICS
RESEARCH**
Open Access

www.adpr-journal.com

[1] C. Rizza, A. Ciattoni, E. Spinozzi, L. Columbo, *Opt. Lett.* **2012**, *37*, 3345.

[2] J. Ding, N. Xu, H. Ren, Y. Lin, W. Zhang, H. Zhang, *Sci. Rep.* **2016**, *6*, 34020.

[3] O. Paul, C. Imhof, B. Lägel, S. Wolff, J. Heinrich, S. Höfling, A. Forchel, R. Zengerle, R. Beigang, M. Rahm, *Opt. Express* **2009**, *17*, 819.

[4] H.-T. Chen, H. Lu, A. K. Azad, R. D. Averitt, A. C. Gossard, S. A. Trugman, J. F. O'Hara, A. J. Taylor, *Opt. Express* **2008**, *16*, 7641.

[5] M. Islam, J. Sultana, M. Biabanifard, Z. Vafapour, M. Nine, A. Dinovitser, C. Cordeiro, B.-H. Ng, D. Abbott, *Carbon* **2020**, *158*, 559.

[6] J. Zhang, Z. Li, L. Shao, F. Xiao, W. Zhu, *Carbon* **2021**, *183*, 850.

[7] H.-T. Chen, W. J. Padilla, M. J. Cich, A. K. Azad, R. D. Averitt, A. J. Taylor, *Nat. Photonics* **2009**, *3*, 148.

[8] A. C. Strikwerda, K. Fan, H. Tao, D. V. Pilon, X. Zhang, R. D. Averitt, *Opt. Express* **2009**, *17*, 136.

[9] M. Kang, T. Feng, H.-T. Wang, J. Li, *Opt. Express* **2012**, *20*, 15882.

[10] Z. Sun, F. Huang, Y. Fu, *Carbon* **2021**, *173*, 512.

[11] Y. Zhao, A. Alù, *Phys. Rev. B* **2011**, *84*, 205428.

[12] L. Cong, W. Cao, Z. Tian, J. Gu, J. Han, W. Zhang, *New J. Phys.* **2012**, *14*, 115013.

[13] L. Zhu, F.-Y. Meng, L. Dong, J.-H. Fu, F. Zhang, Q. Wu, *Opt. Express* **2013**, *21*, 32099.

[14] B. H. Fong, J. S. Colburn, J. J. Ottusch, J. L. Visher, D. F. Sievenpiper, *IEEE Trans. Antennas Propag.* **2010**, *58*, 3212.

[15] K. Bolotin, K. Sikes, Z. Jiang, M. Klima, G. Fudenberg, J. Hone, P. Kim, H. Stormer, *Solid State Commun.* **2008**, *146*, 351.

[16] A. Principi, E. van Loon, M. Polini, M. I. Katsnelson, *Phys. Rev. B* **2018**, *98*, 035427.

[17] D. A. Iranzo, S. Nanot, E. J. C. Dias, I. Epstein, C. Peng, D. K. Efetov, M. B. Lundeberg, R. Parret, J. Osmond, J.-Y. Hong, J. Kong, D. R. Englund, N. M. R. Peres, F. H. L. Koppens, *Science* **2018**, *360*, 291.

[18] K. S. Novoselov, *Science* **2004**, *306*, 666.

[19] A. N. Grigorenko, M. Polini, K. S. Novoselov, *Nat. Photonics* **2012**, *6*, 749.

[20] M. S. Ukhtary, R. Saito, *Carbon* **2020**, *167*, 455.

[21] L. Ju, B. Geng, J. Horng, C. Girit, M. Martin, Z. Hao, H. A. Bechtel, X. Liang, A. Zettl, Y. R. Shen, F. Wang, *Nat. Nanotechnol.* **2011**, *6*, 630.

[22] W. Zhou, J. Lee, J. Nanda, S. T. Pantelides, S. J. Pennycook, J.-C. Idrobo, *Nat. Nanotechnol.* **2012**, *7*, 161.

[23] H. Yan, T. Low, W. Zhu, Y. Wu, M. Freitag, X. Li, F. Guinea, P. Avouris, F. Xia, *Nat. Photonics* **2013**, *7*, 394.

[24] H. Yan, X. Li, B. Chandra, G. Tulevski, Y. Wu, M. Freitag, W. Zhu, P. Avouris, F. Xia, *Nat. Nanotechnol.* **2012**, *7*, 330.

[25] L. Liu, J. Chen, Z. Zhou, Z. Yi, X. Ye, *Mater. Res. Express* **2018**, *5*, 045802.

[26] N. Papasimakis, S. Thongrattanasiri, N. I. Zheludev, F. G. de Abajo, *Light: Sci. Appl.* **2013**, *2*, e78.

[27] D. Chen, J. Yang, J. Huang, W. Bai, J. Zhang, Z. Zhang, S. Xu, W. Xie, *Carbon* **2019**, *154*, 350.

[28] W. Tang, L. Wang, X. Chen, C. Liu, A. Yu, W. Lu, *Nanoscale* **2016**, *8*, 15196.

[29] E. Galiffi, J. B. Pendry, P. A. Huidobro, *ACS Nano* **2018**, *12*, 1006.

[30] I. Silveiro, A. Manjavacas, S. Thongrattanasiri, F. J. G. de Abajo, *New J. Phys.* **2013**, *15*, 033042.

[31] J. Zheng, L. Yu, S. He, D. Dai, *Sci. Rep.* **2015**, *5*, 7987.

[32] N. H. Tu, M. Takamura, Y. Ogawa, S. Suzuki, N. Kumada, *Jpn. J. Appl. Phys.* **2018**, *57*, 110307.

[33] N. H. Tu, K. Yoshioka, S. Sasaki, M. Takamura, K. Muraki, N. Kumada, *Commun. Mater.* **2020**, *1*, 7.

[34] D. Jin, A. Kumar, K. H. Fung, J. Xu, N. X. Fang, *Appl. Phys. Lett.* **2013**, *102*, 201118.

[35] M. Ghezelsefloo, M. K. Moravvej-Farshi, S. Darbari, *J. Phys. Photonics* **2020**, *2*, 035004.

[36] J. Guo, L. Lin, S. Li, J. Chen, S. Wang, W. Wu, J. Cai, T. Zhou, Y. Liu, W. Huang, *Carbon* **2022**, *189*, 596.

[37] J. Guo, Y. Liu, Y. Lin, Y. Tian, J. Zhang, T. Gong, T. Cheng, W. Huang, X. Zhang, *Nanoscale* **2019**, *11*, 20868.

[38] J. Guo, L. Lin, S. Li, J. Chen, S. Wang, W. Wu, J. Cai, T. Zhou, Y. Liu, W. Huang, *Carbon* **2022**, *189*, 596.

[39] C. Baeumer, D. Saldana-Greco, J. M. P. Martirez, A. M. Rappe, M. Shim, L. W. Martin, *Nat. Commun.* **2015**, *6*, 6136.

[40] Z. Xiao, J. Song, D. K. Ferry, S. Ducharme, X. Hong, *Phys. Rev. Lett.* **2017**, *118*, 23.

[41] K. Buse, *Appl. Phys. B: Lasers Opt.* **1997**, *64*, 273.

[42] L. Arizmendi, F. J. Lopez-Barbera, *Appl. Phys. B* **2007**, *86*, 105.

[43] J. Gorecki, V. Apostolopoulos, J.-Y. Ou, S. Mailis, N. Papasimakis, *ACS Nano* **2018**, *12*, 5940.

[44] J. Gorecki, L. Piper, A. Noual, S. Mailis, N. Papasimakis, V. Apostolopoulos, *ACS Appl. Nano Mater.* **2020**, *3*, 9494.

[45] X. Chen, L. Zhang, S. Chen, *Synth. Met.* **2015**, *210*, 95.

[46] C. Mattevi, H. Kim, M. Chhowalla, *J. Mater. Chem.* **2011**, *21*, 3324.

[47] S. Tang, H. Wang, H. S. Wang, Q. Sun, X. Zhang, C. Cong, H. Xie, X. Liu, X. Zhou, F. Huang, X. Chen, T. Yu, F. Ding, X. Xie, M. Jiang, *Nat. Commun.* **2015**, *6*, 6499.

[48] E. M. de Miguel, J. Limeres, M. Carrascosa, L. Arizmendi, *J. Opt. Soc. Am. B* **2000**, *17*, 1140.

[49] A. Puerto, J. F. Muñoz-Martin, A. Méndez, L. Arizmendi, A. Garca-Cabañes, F. Agulló-López, M. Carrascosa, *Opt. Express* **2019**, *27*, 804.

[50] F. Kalkum, K. Peithmann, K. Buse, *Opt. Express* **2009**, *17*, 1321.

[51] M. Calamiotou, N. Chrysanthakopoulos, G. Papaioannou, J. Baruchel, *J. . Appl. Phys.* **2007**, *102*, 083527.

[52] J. Gorecki, N. Klokkou, L. Piper, S. Mailis, N. Papasimakis, V. Apostolopoulos, *Appl. Opt.* **2020**, *59*, 6744.

[53] F. Jabbarzadeh, M. Heydari, A. Habibzadeh-Sharif, *Mater. Re. Express* **2019**, *6*, 086209.

[54] Y. Zhang, T.-T. Tang, C. Girit, Z. Hao, M. C. Martin, A. Zettl, M. F. Crommie, Y. R. Shen, F. Wang, *Nature* **2009**, *459*, 820.

[55] K. Sato, N. Hayashi, T. Ito, N. Masago, M. Takamura, M. Morimoto, T. Maekawa, D. Lee, K. Qiao, J. Kim, K. Nakagahara, K. Wakabayashi, H. Hibino, W. Norimatsu, *Commun. Mater.* **2021**, *2*, 117.

[56] J.-B. Liu, P.-J. Li, Y.-F. Chen, Z.-G. Wang, F. Qi, J.-R. He, B.-J. Zheng, J.-H. Zhou, W.-L. Zhang, L. Gu, Y.-R. Li, *Sci. Rep.* **2015**, *5*, 15285.

[57] S. Y. Zhou, G.-H. Gweon, A. V. Fedorov, P. N. First, W. A. de Heer, D.-H. Lee, F. Guinea, A. H. C. Neto, A. Lanzara, *Nat. Mater.* **2007**, *6*, 770.

[58] G. Giovannetti, P. A. Khomyakov, G. Brocks, P. J. Kelly, J. van den Brink, *Phys. Rev. B* **2007**, *76*, 7.

[59] Z. H. Ni, T. Yu, Y. H. Lu, Y. Y. Wang, Y. P. Feng, Z. X. Shen, *ACS Nano* **2008**, *2*, 2301.